Journal of Chromatography A, 1217 (2010) 8121–8126

Contents lists available at ScienceDirect

Journal of Chromatography A

journal homepage: www.elsevier.com/locate/chroma

Theoretical optimisation of the side-wall of micropillar array columns using computational fluid dynamics

Joris Vangelooven, Gert Desmet*,[1]

Vrije Universiteit Brussel, Department of Chemical Engineering (Transport Modelling & Analytical Separation Science-group), Pleinlaan 2, 1040 Brussels, Belgium

ARTICLE INFO

Article history:
Received 20 May 2010
Received in revised form 30 August 2010
Accepted 4 October 2010
Available online 11 October 2010

Keywords:
Microfluidics
Hydrodynamics
Computation fluid dynamics
Chromatography

ABSTRACT

The present study provides an overview of the ideal side-wall position in micro-pillar array columns for the case of semi-embedded side-walls. The position has been determined using computational fluid dynamics simulations of the flow field in flow domains with different side-wall shifts. Optimal side-wall shift values are presented for a wide range of shapes (cylinders, and diamonds and hexagons with different aspect ratios) and packing densities. Simple linear correlations that allow calculating the optimised side-wall geometries for the different considered variety of shapes and packing densities could be established. Interestingly, only two correlations are needed to represent all investigated cases: one correlation for all diamonds, and one correlation for the cylinders and all hexagons. Compared to the case of a flat side-wall, the minimal feature size on the mask can be increased by a factor of 2.5 in the case of cylindrical pillar bed with external porosity $\varepsilon = 0.4$, implying that that much smaller pillar diameters can be used in the bulk of the bed before the minimal feature size on the mask falls below the lithography resolution.

© 2010 Elsevier B.V. All rights reserved.

1. Introduction

Collocated monolithic support structures (COMOSS) or Micropillar array columns (μPAC's) have a large potential advantage for chromatography and other separation and reaction processes requiring a uniform flow profile and a high contact area [1–5]. However, whereas the current micro-fabrication technologies allow to produce μPAC's with a perfectly uniform bulk region, their over-all degree of band broadening is strongly influenced by the hydrodynamic design of the flow through-pores just beside the side-walls. The importance of a good hydrodynamic design of the side-wall region of μPAC's was already anticipated in the seminal work of the Regnier-group (see Fig. 5 in [6] and Fig. 3 in [7]). Because the side-wall inevitably has a different geometry than the rest of the bed (uninterrupted surface versus a discrete pillar or particle packing) and therefore inevitably has a different surface-to-volume, and hence flow resistance, the occurrence of a deviating local flow resistance near the side-wall is an intrinsic problem in any pressure-driven device [8–10]. The same problem also occurs in packed bed columns, although it is much more obscured there by the packing heterogeneities in the central part of the bed [11].

Dutta and Leighton showed that the presence of sidewalls increases the band-broadening in open-tubular microchannels by a factor of 8, as compared to an infinite channel without sidewalls [8]. For turbulent flows, the presence of the side-wall has an even greater impact as the surface roughness of etched walls causes recirculation zones in the side-wall zone [12]. The present study, however, only relates to laminar flows as $3 \times 10^{-2} > \mathrm{Re} > 3 \times 10^{-4}$. Vervoort et al. concluded after a Computational Fluid Dynamics (CFD) study that for laminar flows, a faulty design of the side-wall region in pressure-driven 2D etched μPAC's can lead to a strong increase of the band-broadening (easily a factor of 2–4) [13].

In [13], it has been shown for the case of a circular-pillar array with external porosity $\varepsilon = 0.4$ that the most obvious and effective solution to this side-wall problem consists of slightly repositioning the side-wall to adapt the flow resistance of the side-wall region so that it equals that of the bulk of the bed. The distance between the most outward row of pillars and the side-wall where this occurs was referred to as the "magical" wall distance, as it is the distance for which also the additional band broadening induced by the side-wall effect disappears.

The present study extends the work presented in [13] to other external porosities (i.e., packing densities) and pillar shapes, using the same methodology as was proposed and validated there. A major difference with the approach adopted in [13] is that now "semi-embedded" side-walls, i.e., side-walls containing a semi-row of pillars (see Fig. 1), are considered instead of flat side-walls. This was done because it was realized that the latter consistently leads to smaller magical side-wall distances than the former.

Abbreviations: AR, Aspect Ratio; COMOSS, COllocated MOnolithic Support Structures; CFD, Computational Fluid Dynamics; μ-PAC, Micro-Pillar Array Column.

* Corresponding author. Tel.: +32 26293617.
E-mail addresses: jvgeloov@vub.ac.be (J. Vangelooven), gedesmet@vub.ac.be (G. Desmet).
[1] Tel.: +32 0 2 629 32 51; fax: +32 0 2 629 32 48.

0021-9673/$ – see front matter © 2010 Elsevier B.V. All rights reserved.
doi:10.1016/j.chroma.2010.10.029

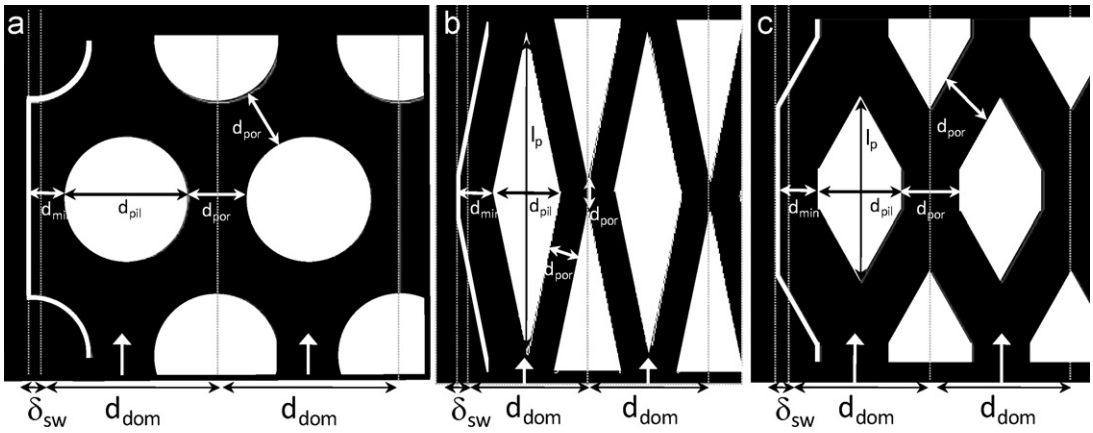

Fig. 1. Investigated geometries (the rightward boundary is a symmetry plane cutting through the center line of the considered channels) and their relevant dimensions. (a) Cylindrical pillars positioned in a grid of equilateral triangles with an inter pillar distance d_{por} and a corresponding domain size d_{dom} (b) diamond-shaped pillars (with AR = ℓ_p/d_p) positioned such that the perpendicular distance between two adjacent pillars equals the axial distance between two subsequent pillars (see two white arrows indicating d_{por}). (c) Hexagonal pillars positioned such that the perpendicular distance between two adjacent pillars equals the axial distance between two subsequent pillars (see two white arrows indicating d_{por}). The vertical dashed lines delimited the adjacent flow domains (with width d_{dom}) of which the total geometry is composed.

Since the magical side-wall distance always scales with the pillar and the through-pore size, and since the magical side-wall distance is always the smallest dimension on the mask, its value also limits the minimal pillar size and minimal through-pore size that can be used. This is an important design issue, because also micro-fabrication processes have their spatial resolution limits. For μPAC's, this implies that the minimal dimension of the interstitial through-pores is determined by the resolution of the UV employed during the photolithography step. Most research institutes are limited to mid-UV light, allowing minimal line widths of about 2 μm. Smaller line widths are possible by using deep-UV light, allowing line widths of about 0.2 μm, but the equipment necessary for this technique is extremely expensive.

Given that the interstitial through-pores in a packed bed of spheres are of the order of 1/3 of the particle diameter, it goes without saying that, in order to be competitive with the current state-of-the-art columns packed with 1.7 or 1.8 μm particles, the through-pores in the bulk of a μPAC should not be larger than some 0.6 μm. However, as already mentioned, the minimal distance on the mask is not the through-pore size in the bulk of the bed but that between the side-wall and the most outward row of pillars (see Fig. 1). For the case of a flat side-wall and bed with circular pillars with $\varepsilon = 0.4$ as studied in [13], this optimal distance is 15% of the pillar size in the bed, while the minimal inter-pillar distance in the bed is about 23% of the pillar size. In other words, to fabricate a bed with an inter-pillar distance of 0.6 μm (corresponding to a pillar with a diameter of 2.6 μm) and with a perfectly flat side-wall, one does not need a photolithographic process with a resolution of 0.6 μm but one with a resolution of 0.4 μm, because the minimal feature size on the mask is not the distance between the pillars in the bed but it is the distance between the last most outward pillars and the side wall. Since a semi-embedded wall has a larger flow resistance than a flat wall, it will always have to be shifted a little bit further (thus creating a larger side-wall through-pore) to achieve the same flow resistance as in the bulk of the bed. As a consequence, the demands on the etching resolution can be somewhat alleviated and the same fabrication process will allow producing arrays with smaller inter-pillar distances.

Briefly, the calculation method to determine the optimal side-wall distance proposed and validated by Vervoort et al. [13] and adopted in the present study is based on the fact that it suffices to position the side-wall such that the mean velocity in the side-wall region (u_{wall}) is equal to the mean velocity in the bulk region of the bed (u_{bulk}). They showed that, if this condition is satisfied, the condition of minimal band broadening is automatically satisfied as well, because the bands no longer feel a different flow resistance and remain perfectly straight up to the side-wall, instead of being warped forward or backward. It should be noted that this condition only holds exactly for the case of non-retained species, or for the case where the retention mainly occurs inside the pillars (which would be the case if the pillars would be fully or meso-porous or would be cladded with a significantly thick meso-porous layer). When the channels are filled with non-porous pillars and when the channel would be uniformly coated with a retentive layer, so that also the flat portions of the side-wall would be coated, the solutions proposed here would still lead to a small difference in retained component velocity between the bulk and the side-wall region of the bed because of the inevitable difference in local surface-to-volume ratio. Solving this appears to be very difficult and will most probably require advanced fabrication techniques that prevent the formation of a retentive layer on the flat portions of the side-wall.

Before proceeding, it is also worthwhile to note that the concept of modifying the side-wall design to achieve a uniform flow resistance over the entire cross-section of the bed is similar to that proposed by Dutta and Leighton [8] and Golay [10] for open-tubular channels with a flat-rectangular cross-section, where they also propose a modification of the side-wall region to obtain the same flow resistance as the bulk of the channel.

2. Considered geometries and employed numerical methods

Fig. 1 shows some of the considered bed and complementary side-wall region designs, as well as the definition of all important characteristic sizes. In total, 3 main types of pillar shapes have been considered: cylinders, diamonds (with different aspect ratio (AR): AR = 1, 2.5 and 5) and hexagons (with AR = 2.5, 5 and 10). For each of these pillar shapes, 5 different external porosities (=ratio of through-pore volume over total bed volume) have been considered (see Table 1). The pillar AR is defined according to the following expression:

$$AR = \frac{\ell_p}{d_{pil}} \tag{1}$$

where ℓ_p is the axial length of the pillar and d_{pil} its transversal width. In the simulations that were conducted to find the optimal side-wall position, the entire side wall has been gradually shifted away from the first row of pillars with a distance δ_{sw}. The differ-

Table 1
A summary of the obtained results for all studied pillar bed geometries.

Shape	AR	d_{por} (μm)	ε	$\delta_{sw,opt}$ (μm)	α_{min}	$\alpha_{sw,opt}$ (μm)	d_{pil} (μm)[a] (1 μm limitation)
Cylinder	1	0.5	0.25	0.10	0.07	0.02	14.16
		1.5	0.46	0.33	0.22	0.07	4.63
		2.5	0.60	0.55	0.36	0.11	2.78
		3	0.65	0.65	0.43	0.13	2.32
		4	0.72	0.89	0.58	0.18	1.73
		10	0.90	2.51	1.50	0.50	0.67
	2.5	0.4	0.13	0.07	0.05	0.01	18.79
		1.5	0.38	0.31	0.21	0.06	4.73
		3.5	0.63	0.79	0.51	0.16	1.97
		12	0.90	3.43	1.89	0.69	0.53
Hexagon	5	0.5	0.12	0.10	0.07	0.02	14.43
		2	0.36	0.43	0.29	0.09	3.49
		4	0.56	0.70	0.54	0.14	1.85
		8	0.74	1.90	1.18	0.38	0.85
		20	0.91	5.81	3.16	1.16	0.32
	10	0.5	0.10	0.10	0.07	0.02	14.41
		1	0.19	0.20	0.14	0.04	7.15
		2	0.32	0.41	0.28	0.08	3.54
		4	0.50	0.82	0.56	0.16	1.77
		8	0.68	1.70	1.14	0.34	0.88
		25	0.90	6.38	3.78	1.28	0.26
Diamond	1	0.25	0.13	0.00	0.03	0.00	39.58
		1	0.39	0.02	0.10	0.00	9.61
		2.5	0.65	0.11	0.27	0.02	3.68
		4	0.77	0.23	0.45	0.05	2.25
		8	0.90	0.62	0.92	0.12	1.08
	2.5	0.3	0.12	0.00	0.03	0.00	33.03
		1	0.31	0.02	0.10	0.00	9.66
		2.5	0.56	0.10	0.27	0.02	3.70
		6	0.78	0.46	0.69	0.09	1.45
		12	0.90	1.53	1.51	0.31	0.66
	5	0.3	0.11	0.00	0.03	0.00	32.43
		1	0.30	0.01	0.10	0.00	9.78
		2.5	0.53	0.07	0.26	0.01	3.80
		6	0.76	0.31	0.66	0.06	1.51
		15	0.90	1.68	1.84	0.34	0.54

[a] d_{pil} value corresponding to geometries where d_{min} is chosen at an assumed etching resolution limit of 1 μm.

ent side-wall geometries for the different considered bed types are indicated in Fig. 1 by the bold lines.

In Fig. 1 all distances of importance when designing the side wall region have been defined. The d_{min} near the side-wall is the smallest distance in the pillar bed, and hence determines (via the etching resolution limits) the minimal pillar size that can be achieved. Further, d_{pil} and d_{por} are respectively the transversal pillar width and the interstitial pore size in the bulk of the pillar bed, and d_{dom} is the lateral domain size of the triangular grid in which the pillars are positioned. For the more elongated structures with an aspect ratio AR > 1, ℓ_p is the axial dimension, defined as in Eq. (1).

All studied geometries were designed such that all inter-pillar distances are equal to d_{por}. In combination with d_{pil}, which was kept constant for all geometries, d_{dom} was calculated according to:

$$d_{dom} = d_{pil} + d_{por} \quad (2)$$

Due to the side wall shift, the domain size is slightly increased in the unity cell closest to the side wall. For a side wall shift δ_{sw}, the minimal dimension d_{min} is defined as:

$$d_{min} = \frac{d_{por}}{2} + \delta_{sw} \quad (3)$$

The different considered flow geometries were drawn using a commercial pre-processing software package (Gambit®). For each geometry, the considered flow domain was 1 unit cell long and 15 unit cells wide. The same software was used to discretize the flow domain. This was done using a tri-mesh meshing scheme. The size and number of grid cells needed to obtain accurate results (determined by the fact that a further decrease in grid cell size only changed the volume-averaged axial velocities by less than 0.5%) was case-dependent. Between 80,000 and 600,000 grid cells were necessary to obtain sufficiently accurate velocity fields. The number depended mostly on the inter pillar distances of the geometry at hand. As a general rule it can be stated that the space between two opposing walls should always be divided in at least 7–10 computational cells to comply with the "0.5%-rule". After this discretisation step, a commercial CFD software package (Fluent® v.6.1.22) was used to calculate the steady-state velocity fields. An implicit steady-state solver was used with second order discretisation for the pressure and momentum calculation and a SIMPLEC discretisation for the pressure–velocity coupling. Periodic boundary conditions were defined to connect the outlet planes to the inlet planes, thus creating and infinitely recirculating and hence infinitely long column, without entry or exit effects for the calculated flow field. A pressure drop per unit length ($\Delta P/L$) of 1×10^5 to 2.5×10^6 Pa/m was defined in order to obtain realistic flow velocities. At one side of the flow domain, a symmetric boundary condition was imposed. This theoretically doubles the width of the model, and was used to express the condition of no-slip at the liquid phase boundaries of the flow domain. At the other side of the flow domain, a fixed-wall boundary condition was imposed on the actual side-walls of the flow domain, represented by the bold line in Fig. 1. The numerical solver was allowed to iterate until the continuity residuals were constant, typically around a value of 10^{-12}.

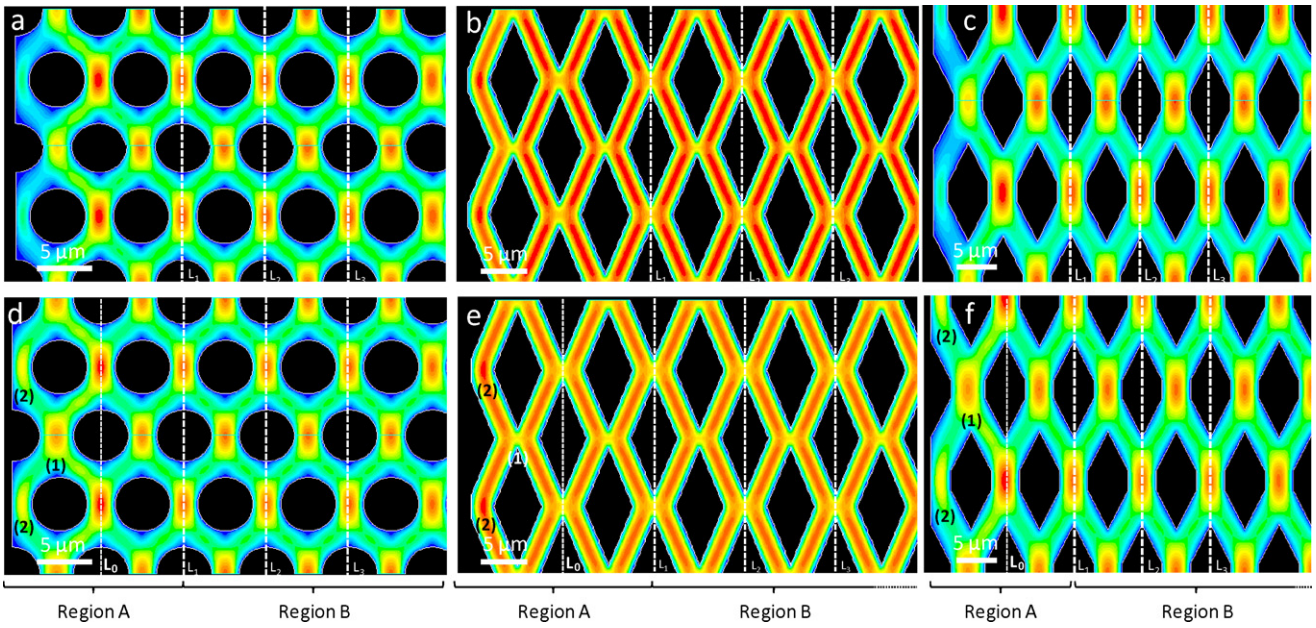

Fig. 2. Velocity fields for the three studied pillar shapes: (a–c) Velocity fields for $\delta_{sw} = 0$ for (a) cylindrical pillars ($d_{pil} = 5\,\mu m$, $d_{por} = 3.5\,\mu m$) (b) diamond-shaped pillars ($d_{pil} = 5\,\mu m$, $d_{por} = 2.5\,\mu m$, AR = 2.5) and (c) hexagonal pillars ($d_{pil} = 5\,\mu m$, $d_{por} = 2.5\,\mu m$, AR = 2.5). (d and e) Velocity fields for $\delta_{sw} = \delta_{sw,opt}$ for the corresponding geometries. The difference between through-pore types (1) and (2), as well as the meaning of the division lines L_0, L_1, L_2, L_3 is discussed in the text.

Using the post-processing possibilities of Fluent®, the average flow velocities in region A (immediately adjacent to side-wall) and region B (bulk of bed) were compared by calculating the surface-averaged axial velocity component over all grid cells in both regions. Fig. 2 also shows the different positions of the division line L (L_1, L_2, L_3) that were considered to split up the bed into the A- and B-regions. The obtained results were subsequently reported as $\Delta u/u_{bulk}$:

$$\Delta u = \frac{u_{sw} - u_{bulk}}{u_{bulk}} \tag{4}$$

with u_{sw} the average fluid velocity in region A and u_{bulk} the average fluid velocity in region B. Obviously, the ideal ("magical") side-wall shift is that for which $\Delta u = 0$.

To find this optimal side-wall shift, velocity fields have been calculated for varying side-wall shifts (δ_{sw}) in an iterative process. First, a global estimation of $\delta_{sw,opt}$ was made by shifting the side-wall with 10, 20 and 30% of the inter pillar distance. Then, a straight line was fitted through a $\Delta u/u_{bulk}$ versus δ_{sw} plot (see examples in Fig. 3 further on). Using this line, an estimation of $\delta_{sw,\,opt}$ was made using the solver function of Microsoft Excel. To validate this estimation, a new flow field were calculated for this new δ_{sw} and four values within 20% of this value (2 larger, 2 smaller), to obtain a more precise estimation for $\delta_{sw,opt}$. Usually, this last value was within 5% of the first estimation. For the few cases where the first global estimation was too far off, and the difference between the two interpolated $\delta_{sw,opt}$-values was larger than 15%, a second iterative step was done to check the accuracy of the obtained $\delta_{sw,opt}$-value.

3. Results and discussion

Fig. 2 shows the calculated velocity fields for some of the considered bed geometries (results for all other considered cases were very similar). For each geometry, 2 different values of the side-wall shift are represented, one with $\delta_{sw} = 0$ (Fig. 2a–c) and one with $\delta_{sw} = \delta_{sw,opt}$ (Fig. 2d and e). Obviously, more values of δ_{sw} were considered (data not shown) and the optimal side-wall shift simulations presented in Fig. 2d and e were performed after the $\delta_{sw,opt}$-value was determined using the approach illustrated in Fig. 3 further on. The cylinder and the hexagonal pillar bed cases with $\delta_{sw} = 0$ in Fig. 2a and c clearly show a strongly reduced flow velocity near the side-wall (cf. the blue coloured regions to the left of the flow domains), as a consequence of the increased wall surface in this region compared to the bulk of the bed. For the diamond-shaped pillar bed, the side-wall effect is much less pronounced. This can be explained by the fact that a unit cell of diamond-shaped pillar beds contains much less "extra" wall surface in the side-wall region. As a consequence, only a small side-wall shift is needed to counter the effect of this increased surface, hence explaining why the difference between the $\delta_{sw} = 0$- and the $\delta_{sw} = \delta_{sw,opt}$-case is very small in the case of diamond pillar beds (compare Fig. 2b with e). The effect obtained by making an optimal side-wall shift on the velocity field of the cylinder and the hexagonal pillar beds is much more pronounced. This can especially be noted from the row of pillars where the through-pore is denoted by the number (1) in Fig. 2d and f. Whereas the flow velocity in this same pore was obviously much smaller than in the rest of the bed for the $\delta_{sw} = 0$-case in Fig. 2a and c, this velocity is now nearly equal to that of the other pores in the bulk of the bed (it is a little bit less because the pore is a little bit wider than the rest of the pores because of the side-wall shift). The velocity in the through-pores denoted by the number (2) in Fig. 2d and f is in the $\delta_{sw} = \delta_{sw,opt}$-case still smaller than in the rest of the bed, but this is due to the fact that the flow in these rows needs to divide over one additional through-pore compared to the rows just above and just below (one half through-pore near the represented side-wall and one half through-pore near the side-wall on the opposite side of the symmetry plane at the outer right line of the represented flow domains). As a consequence, the equilibration of the flow resistance does not occur on the scale of the most outward through-pore, but in the region to the left of the division line L_0, as this covers both the pores of type (1) and that of type (2) and their neighbouring pore.

Fig. 3 shows some example plots of how the $\Delta u/u_{bulk}$-values vary as a function of the relative side-wall shift δ_{sw}/d_{pil} ($=\alpha_{sw}$) for some of the considered bed geometries (results for all other considered cases were very similar), with a positive Δu-value when δ_{sw} is too large, and vice versa. Connecting the lines between the different data points and establishing the intersection with the

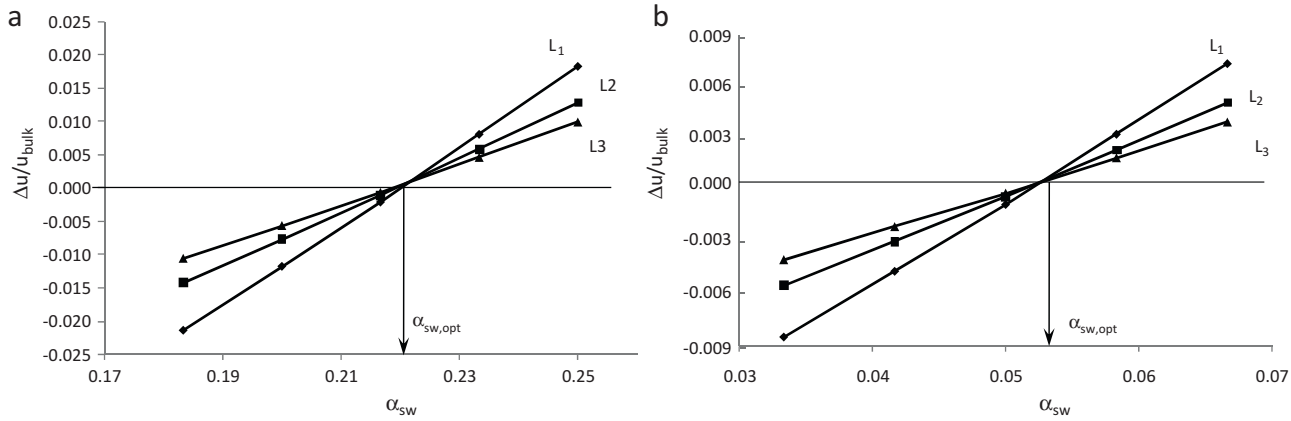

Fig. 3. Plots of $\Delta u/u_{bulk}$-values versus α_{sw} (=δ_{sw}/d_{por}) for (a) cylindrical pillars (d_{pil} = 5 μm, d_{por} = 3 μm, ε = 0.65) and (b) diamond-shaped pillars (d_{pil} = 5 μm, AR = 4, d_{por} = 6 μm, ε = 0.76). $\alpha_{sw,opt}$ was determined for the different lines (L_1, L_2, L_3) that have been considered to divide the flow domain into a side-wall and a bulk region (resp. region A and B).

Δu = 0-line then readily yields the optimal side-wall shift $\delta_{sw,opt}$ (see Experimental for a more accurate description).

A nice feature of the method, as already remarked by Vervoort et al. [13], is that the finally obtained $\delta_{sw,opt}$-value does not depend upon the position of the line used to divide the bed in the side-wall and the bulk region. This can be concluded from Fig. 3 from the fact that the curves for the different L-lines (position, see L_1, L_2, L_3 in Fig. 2) all intersect at the same point, and is in agreement with the fact that, once the flow resistance in the side-wall and the bulk regions is equal, it no longer makes sense to discern two regions, and hence the irrelevance of the position of the division line.

Because of the small feature sizes, the flow conditions in any conceivable μPAC-application lie well within the laminar region, so that the relative magnitude and direction of the velocity field vectors is independent of the mean fluid velocity [14]. Hence, the condition of equal flow resistances between region A and B will always be reached for the same $\delta_{sw,opt}$, implying that the optimal side-wall design is valid for any flow rate and also implying that the determination of $\delta_{sw,opt}$ can be based on one single flow rate. This was checked for a number of different geometries and was always confirmed, as different mean velocities always yielded perfectly coinciding data points in the type of dimensionless $\Delta u/u_{bulk}$ versus α_{sw} plots shown in Fig. 3.

> "Several models have been proposed in literature to estimate the effect of a non-uniform velocity field on the total plate height [5,14]. Expression A.38 from reference 14 allows calculating the effect of different relative velocity differences for a stepwise flat velocity profile, a constant velocity in the pillar bed and a different velocity near the side walls. If we consider the example shown in Fig. 2c in which a velocity difference of 12.7% occurs due to a 700 nm deviation of the side wall position: for a boundary layer thickness of about 1 domain size (10 μm), a radial dispersion of 1×10^{-9} m^2/s [15] and a mean liquid velocity of 5 mm/s, this 12.7% velocity difference leads to an increase in total plate height of 5.8 μm. Compared to the plate height values measured in the central part of the channel in an experimental study, this would lead to, depending on the retention factor, a 50 to 200% increase in plate height values [16]."

Table 1 collects all the different optimal side-wall shift values and reports them as a fraction of the pillar width d_{pil}:

$$\alpha_{opt} = \frac{\delta_{sw,opt}}{d_{pil}} \quad (5)$$

Another useful measure, containing similar information, is the value of α_{min}. This relates the optimal minimal feature size (definition see Fig. 1) to the pillar size:

$$\alpha_{min} = \frac{d_{min}}{d_{pil}} \quad (6)$$

The calculated values for $\delta_{sw,opt}$ and d_{dmin} shown in Table 1 confirm what was already visible in Fig. 2a–c, i.e., the cylindrical and hexagonal pillar beds require much larger side-wall shifts than the diamond-shaped pillars. When α_{min} is plotted versus the dimensionless relative through-pore size ($d'_{por} = d_{por}/d_{pil}$), nearly perfectly linear relationships are obtained for each shape (Fig. 4). Since d_{por}/d_{pil} is a measure that increases with increasing external porosity ε, i.e., with decreasing packing density, the linear increase means that the side-wall needs to be shifted over a relatively larger distance when the bed itself becomes less dense. This can easily be rationalized by the fact that the relative amount of "extra" wall parts near the side-wall increases when the packing density of the bed decreases. This implies that the arresting effect of the side-wall region will be relatively larger in these more dilute beds so that a larger wall shift is needed. On the other hand, in the case of a very dense bed, there is already so much surface in the bed that the "extra" parts of the side-wall are relatively small, so that only a relatively small side-wall shift is needed. Eventually, α_{min} tends to zero when d_{por}/d_{pil} tends to zero. The plots in Fig. 4 have been fitted with a linear relationship and 95% confidence intervals have been calculated using OriginPro 8.0.

Interestingly, the straight-line relationships for the different pillar shapes group into two narrow clusters: one grouping all

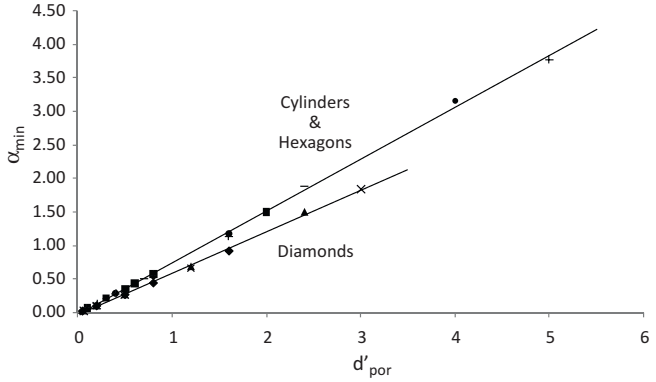

Fig. 4. Plots of α_{min} versus d'_{por} (=d_{por}/d_{pil}) for cylindrical (■) and hexagonal pillars (AR 2.5 (−), 5 (●) and 10(+)) in one cluster and the diamond-shaped pillars (AR 1 (♦), 2.5 (▲) and 5 (×)) in the other.

hexagonal beds (with AR = 2.5, 5 and 10) and the cylindrical beds, and one grouping the three diamond-shaped beds (AR1, 2.5 and 5). The latter cluster has a significantly smaller slope than the former, again reflecting the much smaller side-wall shifts that are needed in the case of diamond-shaped pillars. Fitting both groups of clusters separately, the two following mathematical relationships can be established:

$$\alpha_{min} = 70.06(\pm 0.04) + 0.62(\pm 0.017) d'_{por} (\text{diamonds with AR} = 1, 2.5 \text{ and } 5) \quad (7)$$

$$\alpha_{min} = 0.05(\pm 0.04) + 0.77(\pm 0.016) d'_{por} (\text{cylinders and hexagons with AR} = 2.5, 5 \text{ and } 10) \quad (8)$$

The values between brackets are the values of the calculated 95% confidence intervals for the fitted parameters. Because the results are presented in a dimensionless form, the results in Fig. 4 are valid for the full range of velocities, porosities and pillar dimensions. A plot similar to that shown in Fig. 4 is obtained when $\alpha_{sw,opt}$ is plotted versus d_{por}/d_{pil} (data not shown), as the shapes divide into the same two clustered groups. However, the clustering is slightly less dense and the relationships are slightly curved.

The results in Table 1 now allow calculating the smallest pillar diameter of a given shape still feasible with a given micro fabrication limitation. Multiplying this limiting dimension by the α_{min} value of the pillar shape and porosity of choice results in the minimally feasible d_{pil}. For example, if we assume that a d_{min} of 1 μm is the lower limit of the available micro fabrication processes, the smallest feasible pillar diameter in a cylindrical pillar bed, $\varepsilon = 0.6$ would be 1.39 μm. This exercise is repeated for each considered type of bed in the last column of Table 1, providing the minimal pillar size one can still obtain when the etching limit determining the value of d_{min} would be at 1 μm. If the etching limit would be at 2 μm, the minimal pillar size values would simply be 2 times larger than the values cited in the last column. Interestingly, the cylinders and the hexagonally shaped pillars can, for the same etching limit, be made much smaller than the diamond-shaped pillars. It should be pointed out that if one is to use Eqs. (7) and (8) to calculate α_{min}, it is best, when possible, to consider the expected amount of underetching during the microfabrication step for the estimation of d'_{por}.

Another conclusion that can be made from the obtained results is that a semi-embedded side-wall leads to much larger α_{min}-values than the flat side-wall design considered in [13]. Compared to the results for cylindrical pillars ($\varepsilon = 0.40$), α_{opt} has roughly increased with a factor of 1.65 from 0.15 for a straight side-wall (see [13]) to a value of about 0.24 for an embedded side-wall (value extrapolated for $\varepsilon = 0.40$ using Eq. (8)). This implies that an embedded side-wall design allows fabricating beds with a pillar size that can be made roughly 2.5 times smaller than if a fully flat side-wall would be used. This allows an improvement of the chromatographic performance, as separation efficiency scales inversely with d_{pil}.

4. Conclusions

The difference in flow resistance between the side-wall region and the bulk of the bed in micro-pillar array columns, representing a potential cause of significant additional band broadening, can be perfectly equalized by shifting the side-wall a little bit more outward. If one risks to run into etching resolution limitations, semi-embedded side-walls are to be preferred over fully flat side-walls, as the side-wall distances (d_{min}, see Fig. 1) is the minimal feature size on the mask. For a given pillar size, d_{min} is significantly larger for semi-embedded side-walls than for fully flat side-walls.

Using computational fluid dynamics simulations, optimal side-wall shift could be obtained for a wide range of shapes (cylinders, and diamonds and hexagons with different aspect ratios) and packing densities. Plotting these values as a function of the ratio of inter-pillar distance to lateral pillar width (d_{por}/d_{pil}), a surprisingly simple linear correlation is obtained for each pillar shape. Furthermore, these linear relationships are grouped in two dense clusters: one grouping all diamonds, and one grouping the cylinders and all hexagons.

When attempting to fabricate beds with minimal pillar sizes while still respecting the optimal side-wall distance, beds with cylindrical or hexagonally shaped pillars are to be preferred over diamond-shaped pillars.

Nomenclature

α_{sw}	$\delta_{sw,opt}/d_{pil}$
α_{min}	d_{min}/d_{pil}
ε	external porosity (/)
$\delta_{sw(,opt)}$	(Optimal) side-wall shift (m)
d_{pil}	particle diameter (m)
d_{min}	minimal dimension in column (m)
d_{por}	inter-pillar distance (m)
d'_{por}	ratio of inter-pillar distance over pillar diameter (d_{por}/d_{pil})
d_{dom}	domain size (m)
u_{wall}	velocity in the side-wall region (m/s)
u_{bulk}	velocity in the central region (m/s)

Acknowledgements

J.V. gratefully acknowledges a specialisation grant from the Institute for Science and Technology (IWT) from the Flanders region.

References

[1] A. Fonverne, F. Ricoul, C. Demesmay, C. Delattre, A. Fournier, J. Dijon, F. Vinet, Sens. Actuators B 129 (2008) 510–517.
[2] N.V. Lavrik, L.C. Taylor, M.J. Sepaniak, Lab Chip (2010), doi:10:1039/b920275g.
[3] C. Aoyama, A. Saeki, M. Noguchi, Y. Shirisaki, S. Shoji, T. Funatsu, Anal. Chem. 82 (2010) 1420–1426.
[4] B. He, F. Regnier, J. Pharm. Biomed. Anal. 17 (1998) 925–932.
[5] X. Yan, Q. Wang, H. Bau, J. Chromatogr. A 1217 (2010) 1332–1342.
[6] F.E. Regnier, B. He 6,596,144 U.S. (2003).
[7] B. He, N. Tait, F. Regnier, Anal. Chem. 70 (1998) 3790–3797.
[8] D. Dutta, D.T. Leighton, Anal. Chem. 73 (2001) 504–513.
[9] M. Doshi, P. Daiva, W. Gill, Chem. Eng. Sci. 33 (1978) 795–804.
[10] M.J.E. Golay, J. Chromatogr. A 216 (1981) 1–8.
[11] G. Guiochon, J. Chromatogr. A 1126 (2006) 6–49.
[12] A.S. Rawool, S.K. Mitra, S.G. Kandlikar, Microfluid Nanofluid 2 (2006) 215–221.
[13] N. Vervoort, J. Billen, P. Gzil, G. Baron, G. Desmet, Anal. Chem. 76 (2004) 4501–4507.
[14] K. Broeckhoven, G. Desmet, J. Chromatogr. A 1216 (2009) 1325–1337.
[15] J. Vangelooven, G. Desmet, J. Chromatogr. A 1217 (2010) 6724–6732.
[16] W. De Malsche, H. Eghbali, D. Clicq, J. Vangelooven, H. Gardeniers, G. Desmet, Anal. Chem. 79 (2007) 5915–5926.